Genotype tunes pancreatic ductal adenocarcinoma tissue tension to induce matricellular fibrosis and tumor progression

Hanane Laklai[1], Yekaterina A Miroshnikova[1], Michael W Pickup[1], Eric A Collisson[2], Grace E Kim[3], Alex S Barrett[4], Ryan C Hill[4], Johnathon N Lakins[1], David D Schlaepfer[5], Janna K Mouw[1], Valerie S LeBleu[6], Nilotpal Roy[7], Sergey V Novitskiy[8], Julia S Johansen[9], Valeria Poli[10], Raghu Kalluri[6], Christine A Iacobuzio-Donahue[11], Laura D Wood[12], Matthias Hebrok[7], Kirk Hansen[4], Harold L Moses[8] & Valerie M Weaver[1,13–16]

Fibrosis compromises pancreatic ductal carcinoma (PDAC) treatment and contributes to patient mortality, yet antistromal therapies are controversial. We found that human PDACs with impaired epithelial transforming growth factor-β (TGF-β) signaling have high epithelial STAT3 activity and develop stiff, matricellular-enriched fibrosis associated with high epithelial tension and shorter patient survival. In several KRAS-driven mouse models, both the loss of TGF-β signaling and elevated β1-integrin mechanosignaling engaged a positive feedback loop whereby STAT3 signaling promotes tumor progression by increasing matricellular fibrosis and tissue tension. In contrast, epithelial STAT3 ablation attenuated tumor progression by reducing the stromal stiffening and epithelial contractility induced by loss of TGF-β signaling. In PDAC patient biopsies, higher matricellular protein and activated STAT3 were associated with SMAD4 mutation and shorter survival. The findings implicate epithelial tension and matricellular fibrosis in the aggressiveness of SMAD4 mutant pancreatic tumors and highlight STAT3 and mechanics as key drivers of this phenotype.

PDAC fibrosis compromises drug delivery, impedes immune cell accessibility and promotes disease aggression and therapy resistance[1–4]. Inhibition of stromal sonic hedgehog (SHH) signaling in a mouse model has been shown to significantly reduce fibrosis and increase drug update to stabilize, at least transiently, the disease[5]. Similarly, using hyaluronidase to reduce the abundance of mouse tumor hyaluronan and treating xenografted human pancreatic tumors with an angiotensin inhibitor to reduce tissue tension facilitate chemotherapy delivery[1,6]. But phase 2 clinical trials targeting fibrosis did not increase patient survival[7]. Experiments in mouse models of PDAC revealed that, although depletion of proliferating α-smooth muscle actin (α-SMA)-positive stromal cells reduced fibrosis, the vasculature remained abnormal and the tumors were hypoxic and less differentiated, resulting in accelerated mortality[8]. Additionally, despite a reduction in fibrosis and enhancement of tissue vascularity, genetic ablation of SHH or treatment with a smoothened inhibitor resulted in mouse PDACs that were less differentiated and more aggressive[9].

At first glance, these data imply that the stroma can both promote and restrain tumor progression and suggest stromal dependency may be context dependent. Nevertheless, these experimental and clinical manipulations were based on presumed similarities in tissue across PDACs regardless of tumor genotype; mediation of stromal remodeling in PDACs by a uniform population of stromal fibroblasts; and comparable physical impacts of fibrosis, including the restraint of tumor cells, impedance of tumor-associated vasculature and prevention of immune infiltratation[10–12]. Yet the extent, nature and tumor cell response to tumor-associated fibrosis varies widely across cancers, tumor subtypes and even within the same tumor; the stromal cells that contribute to extracellular matrix (ECM) deposition and remodeling in tumors are heterogeneous[13–16]. Importantly, oncogenic transformation itself increases tumor cell tension, which can critically contribute to ECM remodeling and the malignant phenotype, as was demonstrated by a Ras-transformed epithelium whose ROCK-dependent contractility and fibrosis induction was essential for Wnt-dependent squamous

[1]Center for Bioengineering and Tissue Regeneration, Department of Surgery, University of California, San Francisco, San Francisco, California, USA. [2]Department of Medicine, University of California, San Francisco, San Francisco, California, USA. [3]Department of Pathology, University of California, San Francisco, San Francisco, California, USA. [4]Department of Biochemistry and Molecular Genetics, University of Colorado, Denver, Aurora, Colorado, USA. [5]Department of Reproductive Medicine, University of California, San Diego Moores Cancer Center, La Jolla, California, USA. [6]Department of Cancer Biology, Metastasis Research Center, University of Texas M.D. Anderson Cancer Center, Houston, Texas, USA. [7]Diabetes Center, Department of Medicine, University of California, San Francisco, San Francisco, California, USA. [8]Department of Cancer Biology, Vanderbilt University School of Medicine, Nashville, Tennessee, USA. [9]Department of Oncology, Herlev Hospital, Copenhagen University Hospital, Copenhagen, Denmark. [10]Department of Molecular Biotechnology and Health Sciences, Molecular Biotechnology Center, University of Turin, Turin, Italy. [11]Department of Pathology, David Rubenstein Center for Pancreatic Cancer Research, Human Oncology and Pathogenesis Program, Memorial Sloan Kettering Cancer Center, New York, New York, USA. [12]Gastrointestinal and Liver Pathology Department, Johns Hopkins University, Baltimore, Maryland, USA. [13]Department of Anatomy, University of California, San Francisco, San Francisco, California, USA. [14]Department of Bioengineering and Therapeutic Sciences, University of California, San Francisco, San Francisco, California, USA. [15]Eli and Edythe Broad Center of Regeneration Medicine and Stem Cell Research, University of California, San Francisco, San Francisco, California, USA. [16]Helen Diller Comprehensive Cancer Center, University of California, San Francisco, San Francisco, California, USA. Correspondence should be addressed to V.M.W. (valerie.weaver@ucsf.edu).

carcinoma progression[17–19]. Sorting out the contribution of stromal and epithelial elements to PDAC fibrosis and pathology would go far in guiding the development and application of antistromal therapies.

Patients whose tumors harbor mutations in mothers against DPP homolog 4 (SMAD4) die more frequently from disseminated disease[20], and reduced levels of epithelial SMAD4 were shown to enhance the aggressiveness and dissemination of tumor cells from PDACs in an experimental mouse model[21]. Interestingly, experimental tumors with combined *Kras* mutations and *Tgfbr2* deletion are highly fibrotic and exhibit a pronounced mesenchymal-like phenotype following stromal ablation[8,22]. Clinically, patient PDACs with a quasi-mesenchymal phenotype are more aggressive and resistant to treatment than PDACs with a classical, more differentiated histophenotype[23,24]. Moreover, mesenchymal-like patient PDACs are often associated with aberrant TGF-β signaling in the epithelium[25]. These findings suggest that PDACs in which TGF-β signaling is compromised may have a unique stromal-epithelial interaction phenotype that could influence their response to antistromal therapies. As such, we investigated the interplay between tumor genotype and fibrotic phenotype in PDAC progression.

RESULTS

Tissue tension and collagen thickness link to PDAC prognosis

Fibrillar collagen has been implicated in PDAC aggression and treatment resistance[26], yet recent findings suggest collagen abundance in PDAC may be associated with better, not worse, patient prognosis and with a more differentiated PDAC phenotype[27–29]. We constructed a gene list of major fibrillar collagens (**Supplementary Table 1**) and used this signature to stratify publicly available PDAC data (GEO GSE21501). We found no significant association between expression of the major fibrillar collagens and patient survival. However, when we stratified patient data according to expression of collagens Col1α2, Col2α1 and Col4α1, we found that patients expressing high levels of these specific collagens had lower overall survival (log–rank $P \leq 0.04$) (**Supplementary Fig. 1a**).

To investigate the relationship between fibrillar collagen and PDAC phenotype, we assessed total and fibrillar collagen in PDAC tissue arrays with well-differentiated ($n = 19$), moderately differentiated ($n = 23$) and poorly differentiated ($n = 26$) tumors. Although total and fibrillar collagens were similar in all tumor biopsies regardless of differentiation status (**Fig. 1a** and **Supplementary Fig. 1b,c**), we noted a reduction in number of α-SMA-positive cells in the poorly differentiated PDAC tumor biopsies, compared to the well-differentiated and moderately differentiated tumors[8,30] (**Fig. 1a**) ($P \leq 0.05$). Moreover, the diameter of the collagen fibers adjacent to the epithelial lesions was significantly greater in the poorly differentiated PDACs (**Fig. 1**) ($P \leq 0.01$–0.001). We also detected a progressive increase in level of phosphorylated myosin light chain-2 (p-MLC2) in the epithelium adjacent to the thicker collagen fibers in the moderately and poorly differentiated tumors, which is consistent with increased epithelial actomyosin tension (**Fig. 1a**) ($P \leq 0.05$–0.001) and suggests that an association may exist between tumor cell tension and the architecture of the adjacent collagen bundles[19,31].

To investigate the relationship between fibrillar collagen, epithelial tension and patient survival, we stratified PDAC tumors from a cohort

Figure 1 Tissue tension and collagen thickness linked to PDAC prognosis. (**a**) Hematoxylin and eosin (H&E) and trichrome staining (inset); immunofluorescence images and quantifications (right) of α-SMA, p-MLC2, p-SMAD2 and DAPI; polarized light images of picrosirius red (PR) within the main stroma (PS-MS) and periductal stroma (PS-DS, inset); and second harmonic generation (SHG) of periductal collagen and diameter color-coded SHG in PDAC tissue arrays of well-differentiated ($n = 19$) and moderately ($n = 23$) and poorly differentiated ($n = 26$) tumors. (**b**) H&E and trichrome (inset) staining; immunofluorescence and quantification of α-SMA, p-MLC2, p-SMAD2 and DAPI; PR staining within MS and DS (inset); and periductal SHG and diameter color-coded SHG in tissue from PDAC patients with a median short survival of 11–289 d ($n = 29$) and median long survival of 1,090–3,298 d ($n = 28$). (**c**) H&E staining; PR staining (PS) and quantification within MS and DS; force maps and quantification of the MS and DS (inset); SHG of periductal collagen and diameter color-coded SHG; and immunofluorescence staining and quantification of p-MLC2 and DAPI in PDAC tissue bearing wild-type (WT; $n = 10$) or mutant SMAD4 ($n = 10$). Error bars, mean ± s.e.m. *$P < 0.05$; **$P < 0.01$; ***$P < 0.001$; ****$P < 0.0001$, unpaired two-sided Student's *t*-tests or one-way ANOVA with Tukey's method for multiple comparisons. Scale bars for **a** and **b** are as follows: H&E, 100 μm; trichrome, 50 μm; α-SMA, p-MLC2, p-SMAD2 and DAPI, 75 μm (main) and 40 μm (inset); PS-MS, 50 μm; PS-DS, 40 μm; SHG and fiber diameter, 75 μm. Scale bars for **c** are: H&E, 100 μm; MS and DS, 50 μm; SHG, fiber diameter and p-MLC2 and DAPI, 75 μm. a.u., arbitrary units.
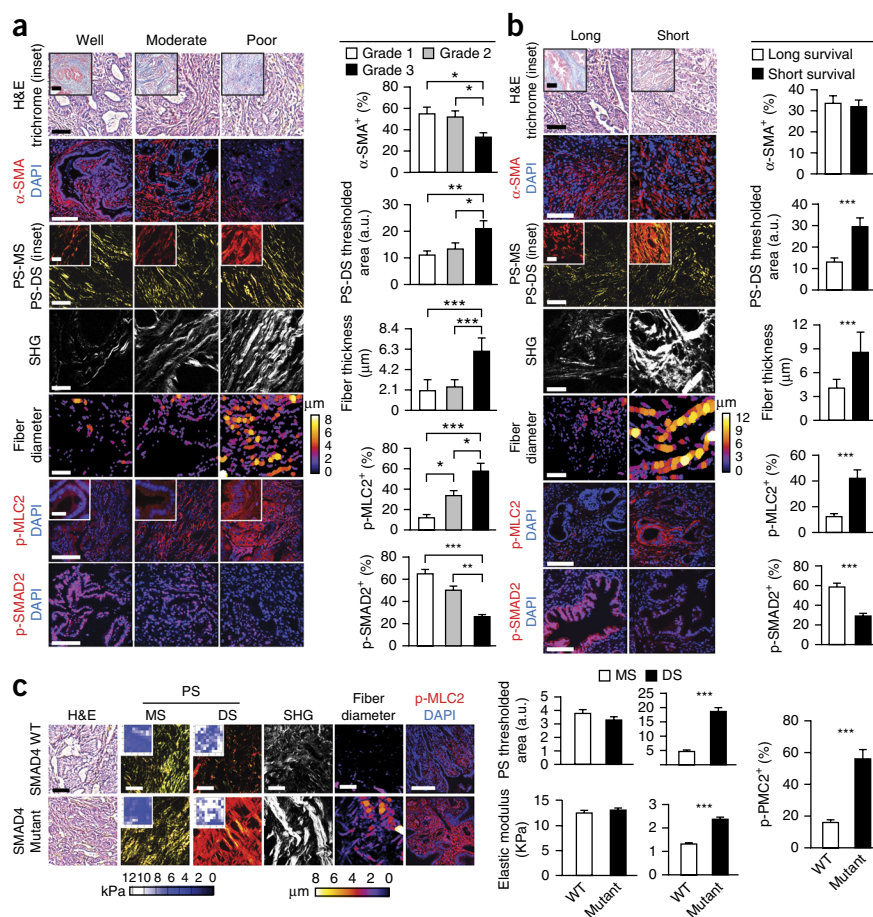
Figure 2 PDAC genotype tunes epithelial tension to regulate fibrosis. (**a**) SHG images and force maps (top insets) from AFM PDAC ECM; immunofluorescence images of p-MLC2, p-MyPT1 (inset), β1-integrin and ^{397}PTK2, YAP1 and DAPI; tenascin C, fibronectin (FN, inset), collagen type XII α1 (collagen 12) and DAPI from 20-week-old KC, KPC or KTC transgenic pancreatic tissues. Scale bars are as follows: SHG, 75 μm; p-MLC2, β1-integrin and ^{397}PTK2, YAP1 and DAPI, 50 μm; tenascin C, collagen type XII α1 and DAPI, 75 μm. (**b**) Quantification of SHG fibril thickness and distribution around PDAC lesions. (**c**) Distribution of PDAC ECM stiffness measured by AFM. (**d**) Percentage of cells expressing tenascin C, fibronectin and collagen 12 for images shown in **a**. (**e**) Quantification of traction force in KC, KPC and KTC cells on 2,300-Pa polyacrylamide gels. (**f**) Mean collagen fiber diameter at 24 h in 3D collagen gels with KC, KPC or KTC cells or with KTC cells treated with vehicle or ROCK inhibitor Y27632. (**g**) Picrosirius red (PR) staining of tissue excised from nude mice 3 weeks after injection with KC, KPC or KTC cells expressing either a control shRNA or an shRNA to ROCK1 (top; scale bar, 75 μm) and immunofluorescence of p-MLC2 and p-MyPT1 (inset), tenascin C, YAP1 and DAPI (scale bars, 50 μm). (**h**) Quantification of stiffness of tissue in **e**. (**i**) Quantification of total fibrillar collagen. For *in vitro* bar graphs (**e,f,h,i**), three technical replicates were analyzed, and results are the mean ± s.e.m. of three independent experiments. For *in vivo* experiments (**a**–**d,g**–**i**), $n = 5$ mice per group. *$P < 0.05$; **$P < 0.01$; ***$P < 0.001$, ****$P < 0.0001$, unpaired two-sided Student's *t*-test, one-way ANOVA with Tukey's method for multiple comparisons or log–rank (Mantel–Cox) test (for survival analysis).
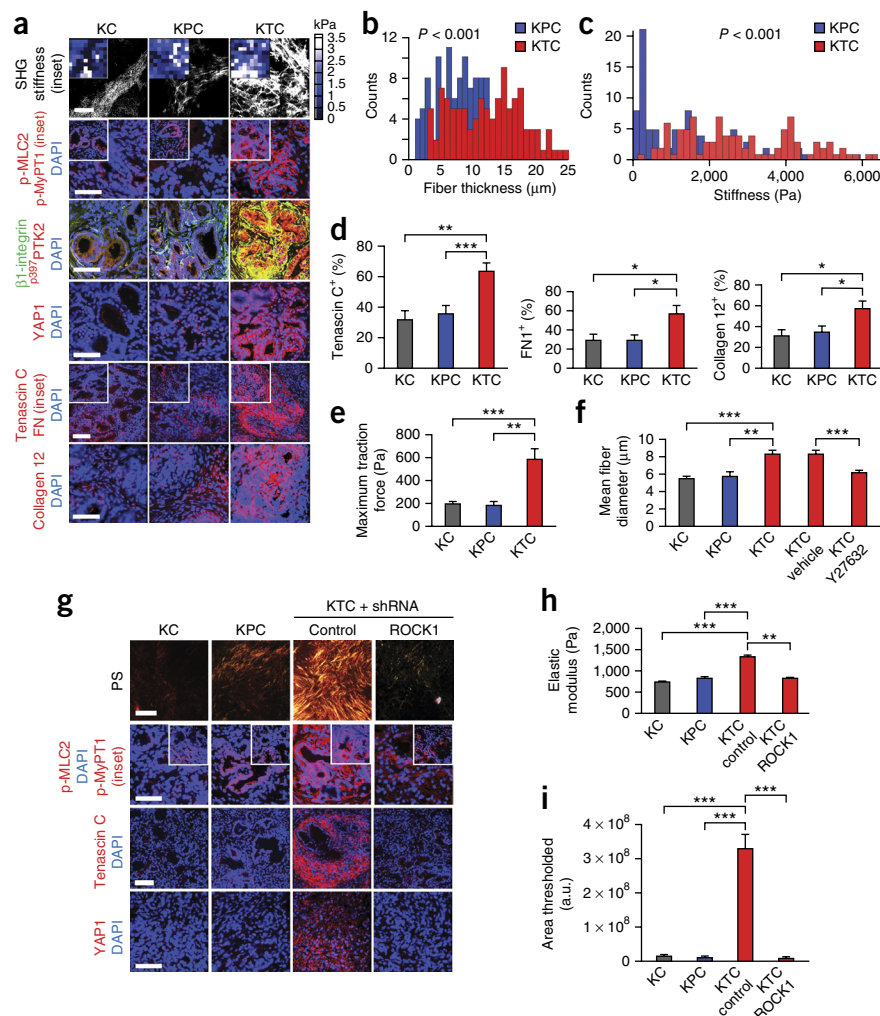
of patients[32] by survival (median survival <10 months versus median survival >24 months). Again, we found no association between total and fibrillar collagen or α-SMA-positive cells and patient survival (**Fig. 1b** and **Supplementary Fig. 1d,e**). However, the diameter of the collagen fibers adjacent to the pancreatic lesions was significantly thicker in patients with the shortest survival (**Fig. 1b**) ($P \le 0.001$). We also observed elevated p-MLC2 in the PDAC tissues from patients with the shortest survival, indicating increased actomyosin tension and a relationship between the contractile PDAC epithelium and the reorganized collagen bundles (**Fig. 1b**) ($P \le 0.001$).

TGF-β signaling is often attenuated in patient PDACs[33], thus we assessed phosphorylation of SMAD2 (p-SMAD2) as a primary mediator of canonical TGF-β signaling. We detected less p-SMAD2 in the least-differentiated PDAC lesions (**Fig. 1a**) ($P \le 0.001$) and the PDACs derived from the patients with the shortest survival (**Fig. 1b**) ($P \le 0.001$), suggesting they had compromised TGF-β signaling[34,35]. Next, we compared the stromal phenotype of patient PDACs with genetically altered SMAD4 to PDACs with wild-type SMAD4 (ref. 36). Although total collagen and α-SMA levels were similar between the cohorts (**Supplementary Fig. 1f**), we observed elevated epithelial p-MLC2 (**Fig. 1c**) ($P \le 0.001$) with increased adjacent collagen fibers in PDACs lacking functional SMAD4 (**Fig. 1c**). Atomic force microscopy (AFM) mechanical testing revealed that the thickened, epithelial-adjacent collagen fibers were stiffer in the PDACs

from patients whose lesions lacked a functional SMAD4 (**Fig. 1c**) ($P \le 0.001$). These findings indicate that the architecture and mechanics of collagen fibers adjacent to the epithelial lesion, and not bulk collagen abundance, may be an indicator of PDAC aggression and that a reduction in TGF-β signaling in the PDAC epithelium may influence the nature of the stromal response.

PDAC genotype tunes epithelial tension to regulate fibrosis

To explore the relationship between TGF-β signaling, collagen organization and tissue mechanics, we exploited three genetically engineered PDAC mouse models: KC (*Kras*$^{LSL-G12D/+}$*Ptf1α*-Cre)[37], KPC (*Kras*$^{LSL-G12D/+}$*Tp53*$^{R172H/+}$*Pdx1*-Cre) and KTC (*Kras*$^{LSL-G12D/+}$ *Tgfbr2*$^{flox/+}$*Ptf1a*-Cre, which bears a *loxP*-flanked allele of *Tgfbr2*) mice. By age 20 weeks, KC mice had progressed to pancreatic intraepithelial neoplasia (PanIN) lesions, whereas KPC and KTC mice developed PDAC lesions[22,38]. Coincident with tumor formation, the pancreatic tissues of both KPC and KTC mice were highly fibrotic, as indicated by abundant total and fibrillar collagen (data not shown). Targeted proteomics confirmed that many fibrillar collagens in KTC and KPC mice were present at similar levels (**Supplementary Table 2**). Immunofluorescence staining showed that KTC and KPC tumors had similar stromal levels of collagen III, α-SMA and fibroblast-activated protein (FAP) (**Supplementary Fig. 2a**). GLI family zinc finger 1 (GLI1), which regulates PDAC fibrosis, was abundantly
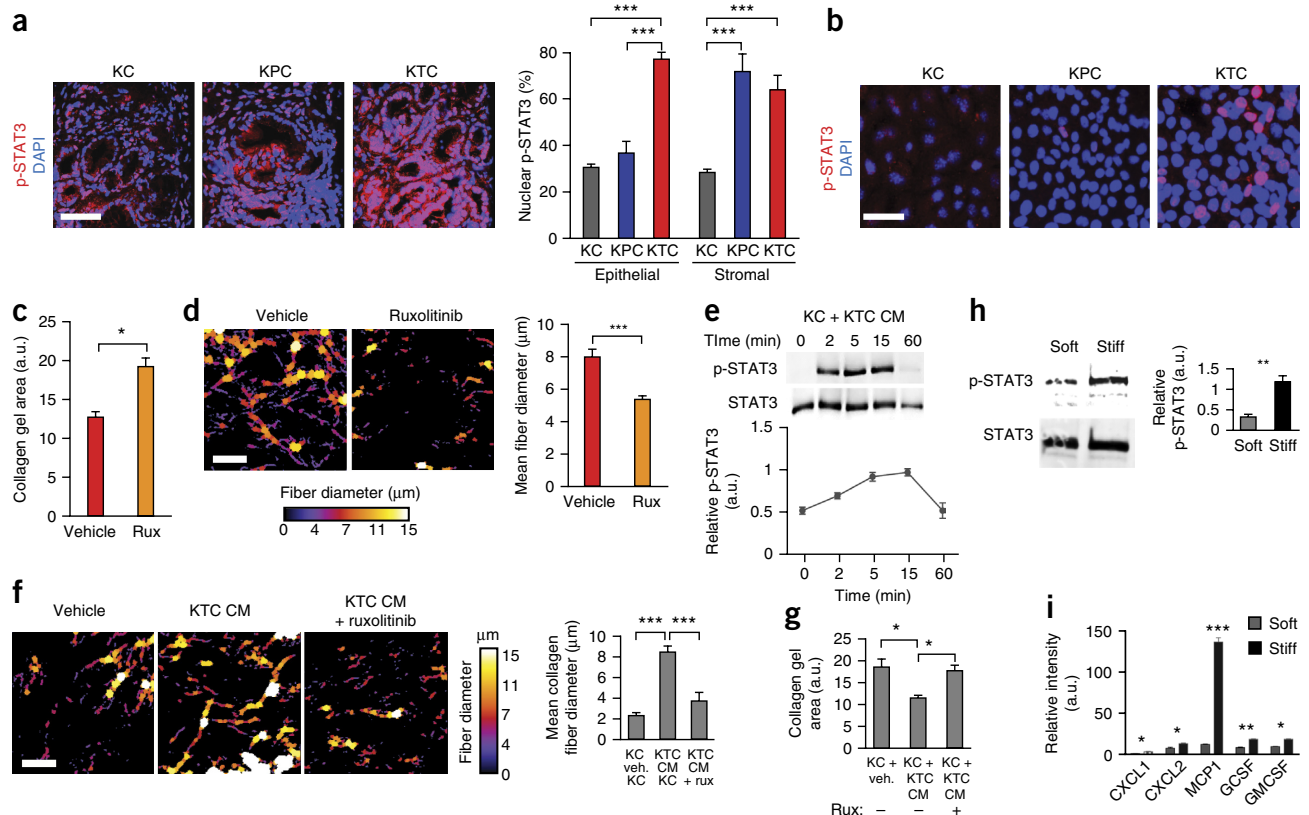
Figure 3 JAK-STAT3 signaling drives ECM remodeling and stiffening. (**a**) Immunofluorescence images (left) and quantification (right) of p-STAT3 and DAPI staining in epithelial and stromal tissue from 20-week-old KC, KPC and KTC mice; scale bar, 50 μm. (**b**) p-STAT3 and DAPI staining of tumor cells from KC, KPC and KTC mice; scale bar, 25 μm. (**c**) Collagen contraction, measured by total collagen gel area in 3D collagen gels with KTC tumor cells treated for 24 h with vehicle or ruxolitinib (rux). (**d**) Polarized light images and quantification of picrosirius red (PR)-stained color-coded fibrillar collagen diameter on gels from **c**; scale bar, 75 μm. (**e**) Immunoblot analysis and relative quantification of p-STAT3 in KC cells after exposure to KTC-conditioned medium (CM). (**f**) Total collagen gel area of gels with KC tumor cells incubated with vehicle (veh), KTC CM or KTC CM and ruxolitinib for 48 h. (**g**) Polarized light images and quantification of PR, color-coded fibrillar collagen diameter; scale bar, 75 μm. (**h**) Immunoblot analysis and quantification relative to total STAT3 and p-STAT3 in KC tumor cells cultured on soft or stiff polyacrylamide substrates. (**i**) Quantification of cytokine levels in the CM of KC cells cultured on soft or stiff polyacrylamide substrates relative to positive controls on the blots. For *in vitro* quantification (**b**–**i**), data are mean ± s.e.m. of three independent experiments, each with three technical replicates. For *in vivo* experiments (**a**), n = 5 mice per group. *$P < 0.05$; **$P < 0.01$; ***$P < 0.001$; ****$P < 0.0001$, unpaired two-sided Student's t-test or one-way ANOVA with Tukey's method for multiple comparisons. a.u., arbitrary units.

and uniformly expressed in the KPC and KTC tumor stroma (**Supplementary Fig. 2a**). Nevertheless, and in agreement with our clinical findings, KTC PDAC lesions had thicker collagen bundles and a stiffer ECM in the periductal region (**Fig. 2a**–**c**) ($P \leq 0.001$). Mass spectrometry and immunofluorescence analyses of the tumor ECM further revealed that the altered fibrillar collagen phenotype and the elevated ECM stiffness in KTC PDAC lesions was accompanied by a significant increase in tenascin C, fibronectin and collagen type XII α1 ($P \leq 0.05$) (**Supplementary Fig. 3b**, **Supplementary Table 2** and **Fig. 2a,b**). The KTC PDAC epithelium was also more contractile, as indicated by more p-MLC2 and myosin phosphatase target subunit 1 (p-MyPT1) (**Fig. 2a** and **Supplementary Fig. 3a**) ($P \leq 0.01$–$0,001$) and higher mechanosignaling, as indicated by activated β1-integrin, phosphorylated focal adhesion kinase ($P^{397}PTK2$) (**Fig. 2a** and **Supplementary Fig. 3a**) ($P \leq 0.05$–0.01) and nuclear Yorkie activated protein (YAP1)[39] (**Fig. 2a** and **Supplementary Fig. 3a**) ($P \leq 0.01$–0.001). These data suggest that a reduction in TGF-β signaling increases actomyosin tension and mechanosignaling in a transformed pancreatic epithelium to induce a stiffer, periductal, matricellular-enriched fibrosis.

We next assessed the contractility phenotype of individual PDAC epithelial cells derived from KC, KTC and KPC mice using traction force microscopy (TFM). KTC tumor cells were more contractile than the KPC or KC cells (**Supplementary Fig. 3c**). KTC tumor cells promoted more Rho kinase-1 (ROCK1)-dependent but not ROCK2-dependent 3D collagen gel contraction than KPC or KC tumor cells (**Supplementary Fig. 4a**) ($P \leq 0.01$–0.001) (**Fig. 2d** and **Supplementary Fig. 5a**–**d**). The KTC tumor cells exhibited higher ROCK1-dependent tumor growth (**Supplementary Fig. 4d**). Myosin tension, as indicated by elevated traction force as well as p-MLC2 (**Fig. 2e** and **Supplementary Fig. 4c**), induced more nuclear YAP1 and YAP activity, as indicated by higher *Ctgf* expression (**Supplementary Fig. 4f**), and promoted greater fiber diameter (**Fig. 2f**). Fibers were also stiffer and enriched for the matricellular protein tenascin C (**Fig. 2g**–**i**) upon orthotopic injection of KTC cells into the pancreas of immunocompromised mice. These data demonstrate that a reduction of TGF-β signaling in the pancreatic epithelium increases tumor cell tension to induce a stiffer, matricellular fibrosis.

KTC tumor cells also showed a significant increase in anchorage-independent growth and colony formation (**Supplementary Fig. 4f**) ($P \leq 0.05$–0.001), which is consistent with a reduced dependence

on ECM ligation for tumor cell survival and the enhanced metastasis incidence observed in patients with mutant SMAD4 (refs. 20,40). However, the size of the KTC tumors was significantly smaller ($P < 0.0001$) than those formed by KPC cells (**Supplementary Fig. 4d,e**). Thus, although pancreatic transformation is universally accompanied by progressive fibrosis and stiffening of the ECM, the nature of the fibrotic response and the mechanophenotype of the cancer can be modified by the genotype of the tumor.

JAK-STAT3 signaling drives ECM remodeling and stiffening

We next sought to clarify how reduced TGF-β signaling could increase tumor cell tension. G-protein-coupled-receptor-mediated Janus kinase (JAK) activation stimulates activation of both signal transducer and activator of transcription-3 (STAT3) and ROCK1 and induces acto-myosin-mediated cell contractility, and STAT3 has been implicated in PDACs[41–45]. We observed significantly more p-STAT3 ($P \leq 0.001$) in the pancreatic epithelium of KTC mice than in KPC or KC mice (**Fig. 3a**), even in PanINs from 8-week-old mice, where the amount of infiltrating immune cells was very low (**Supplementary Fig. 6a**). Although both the stroma and the PDACs in KPC and KTC mice stained positively for p-STAT3 (coincident with an abundant immune infiltrate)[45], p-STAT3 was significantly higher ($P \leq 0.001$) only in the tumor pancreatic epithelium in KTC mice (**Fig. 3a**). We also detected abundant p-STAT3 *in vitro* in nonstimulated KTC, but not KPC or KC, cells (**Fig. 3b** and **Supplementary Fig. 5a**). KTC tumor cell contraction and remodeling of collagen gels was blocked by treatment with the JAK inhibitor ruxolitinib (**Fig. 3c,d** and **Supplementary Fig. 6b**). We cultured

KTC cells for 48 h, collected the medium (conditioned medium) and used it to treat KC cells. We noted that the conditioned medium activated p-STAT3 in cultured KC cells (**Fig. 3e**) and simultaneously increased the JAK-dependent ability of the KC cells to contract and remodel collagen gels (**Fig. 3f** and **Supplementary Fig. 6c**). A stiff ECM can enhance STAT3 activation[46], and we observed higher steady-state p-STAT3 levels in KC tumor cells and higher levels of secreted cytokines in KTC-conditioned medium when they were plated on a stiff ECM (**Fig. 3f–i** and **Supplementary Fig. 6d–f**). These findings identify an epithelial JAK-ROCK-STAT3 signaling circuit as a candidate KTC tumor-cell-specific contractility mechanism that could induce ECM remodeling and foster the development of matricellular-enriched pancreatic fibrosis.

Tumor cell tension accelerates PDAC progression in mice

To test links between p-STAT3, tumor tension and fibrosis in PDAC progression, we crossed transgenic mice expressing *Ptf1α*-Cre with mice expressing a conditional V737N mutation in β1-integrin (β1-V737N mice) (**Supplementary Fig. 7a**), which recapitulates tension-dependent integrin clustering and promotes focal adhesion signaling and ROCK-dependent cell contractility in the pancreatic epithelium[18,47,48]. Immunofluorescence staining in the resulting β1-V737N mice confirmed elevated PTK2 activity ($P \leq 0.001$) in the pancreatic epithelium and revealed higher epithelial contractility, as indicated

Figure 4 Tumor cell tension accelerates PDAC progression in mice. (**a**) Mouse manipulations used to study the impact of increasing pancreatic epithelial cell mechanosignaling using β1-V737N on KRAS-induced pancreatic malignancy. (**b**) Immunofluorescence staining and quantification of p397PTK2, p-MLC2, tenascin C, YAP1, p-STAT3 and CD68; polarized light images of picrosirius red staining and force maps of ECM stiffness in pancreatic tissue from 3-month-old KC and KC/β1-V737N mice. Scale bars are as follows: CD68, 50 μm; p397PTK2, p-MLC2, tenascin C, YAP1 and p-STAT3, 100 μm; PS staining, 75 μm. (**c**) Alcian blue and hematoxylin and eosin (H&E) staining of KC and KC/β1-V737N pancreatic tissue. Scale bars, 100 μm. (**d**) Quantification of histopathologic phenotypes present in KC and KC/β1-V737N mice. (**e**) Polarized light images and quantification of picrosirius red staining (scale bar, 75 μm) and immunofluorescence staining and quantification of tenascin C (scale bar, 75 μm), YAP1 (scale bar, 75 μm), p-STAT3 (scale bar, 25 μm) and DAPI in pancreatic tissue from nude mice injected with KTC tumor cells expressing either a scramble (control) shRNA or a shRNA against PTK2 (shPTK2). (**f**) Quantification of average elastic modulus (Pa) of control and PTK2 knockdown orthotopic tumors. For *in vivo* experiments (**a–f**), n = 5 mice per group. *$P < 0.05$; **$P < 0.01$; ***$P < 0.001$; ****$P < 0.0001$, unpaired two-sided Student's t-tests.
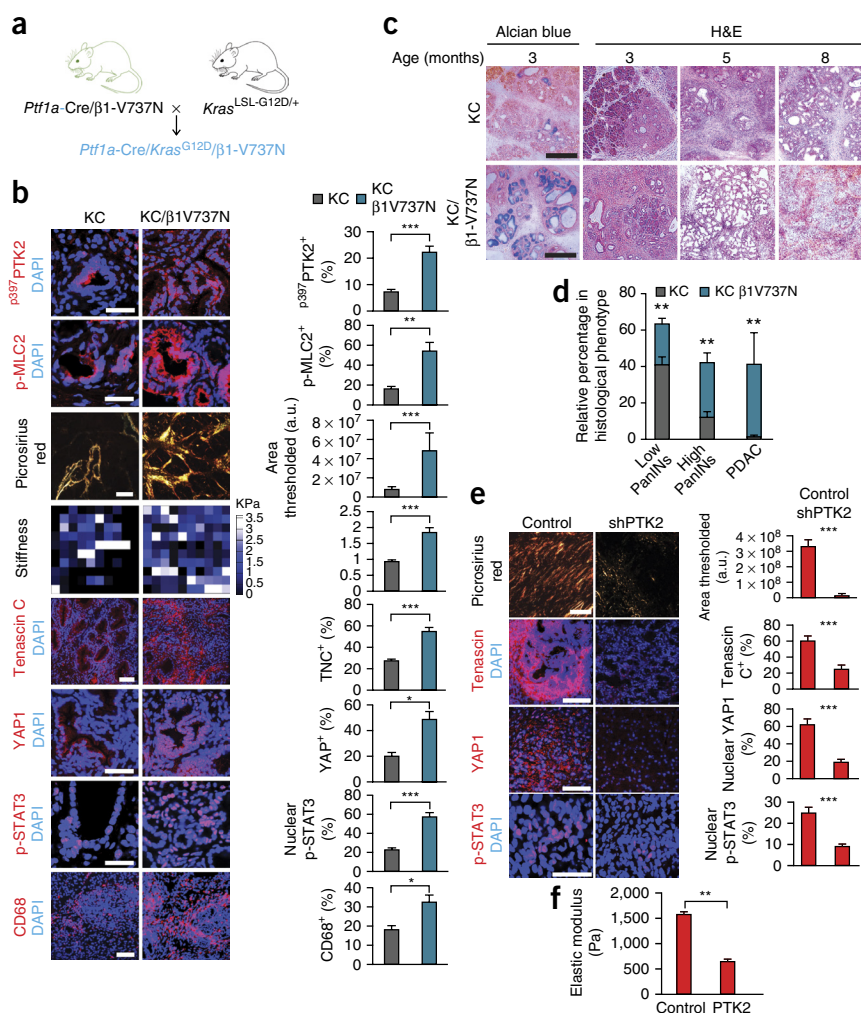
Figure 5 STAT3 induces fibrosis and accelerates PDAC. (**a**) Mouse crosses used for the activated STAT3C manipulations. (**b**) Immunofluorescence images and quantification of pancreatic tissues from 5-week-old KC and KC/STAT3C mice stained for p-STAT3 (scale bar, 75 μm), ^{p397}PTK2 and p-MLC2 (scale bars, 50 μm) and CD68 (scale bar, 100 μm) and polarized light images and quantification of picrosirius red (scale bar, 75 μm) and hematoxylin and eosin (H&E) staining (scale bar, 100 μm). (**c**) Kaplan–Meier survival curves for KC and KC/STAT3C mice. (**d**) Quantification of elastic modulus (Pa) of pancreatic tissue from KC and KC/Stat3C mice shown in **b**. (**e**) Mouse crosses used for the STAT3 knockout studies. (**f**) Immunofluorescence images and quantification of p-STAT3 (scale bar, 75 μm), ^{p397}PTK2 and p-MLC2 (scale bars, 50 μm), tenascin C (scale bar, 100 μm), CD68 (scale bar, 100 μm) and YAP1 (scale bar, 50 μm) and polarized light images and quantification of picrosirius red (scale bar, 75 μm) and H&E (scale bar, 100 μm) staining in pancreatic tissue from 5-week-old KTC-KO (control) and KTC-KO/STAT3-KO mice. (**g**) Kaplan–Meier survival curves for KTC-KO and KTC-KO/STAT3-KO mice. (**h**) Quantification of ECM stiffness on tissue in **f**. For *in vivo* experiments (**a**–**h**), $n = 5$ mice per group. Error bars, mean ± s.e.m. *$P < 0.05$; **$P < 0.01$, ***$P < 0.001$, ****$P < 0.0001$, unpaired two-sided Student's *t*-test.

by increased p-MLC2 ($P \leq 0.001$), and higher mechanosignaling, as indicated by nuclear localization of YAP targets including *Ctgf* ($P \leq 0.05$; **Supplementary Fig. 7b,c**). Evidence of fibrosis was indicated by increased picrosirius red staining (**Supplementary Fig. 7b**), and second-harmonic generation revealed thicker, denser collagen (data not shown). AFM mechanical testing showed a significant ($P \leq 0.001$) stiffening of the ECM surrounding the ductal epithelium (**Supplementary Fig. 7b**). The presence of p-STAT3-positive pancreatic epithelial cells in β1-V737N mice ($P \leq 0.05$), even in the absence of activating oncogene or pre-existing inflammation, confirmed that epithelial tension can directly enhance STAT3 activation, altered cytokine expression and immune cell infiltration (**Supplementary Fig. 7b–e**). Consistently with these results, treatment of the β1-V737N mice with a PTK2 inhibitor reduced p-STAT3, ^{p397}PTK2 and p-MLC2 abundance as well as matricellular-enriched fibrosis (**Supplementary Fig. 8a**). Orthotopic injection of KTC cells expressing a short hairpin RNA (shRNA) against PTK2 (**Supplementary Fig. 9a,b**) into immunocompromised mice also reduced fibrosis ($P \leq 0.001$), decreased stiffness ($P \leq 0.01$) and lowered tenascin C levels ($P \leq 0.001$) toward those of control tumors. The pancreatic tumor epithelium expressing shRNA against *Ptk2* was less mechanically activated than tissue expressing scramble shRNA (controls), as indicated by reduced nuclear YAP1 ($P \leq 0.001$), and had lower levels of nuclear p-STAT3 ($P \leq 0.001$) (**Fig. 4**) than control tumors.

To assess the relationship between epithelial tension and PDAC development, we bred Ptf1a-Cre/β1-737N mice with KC mice
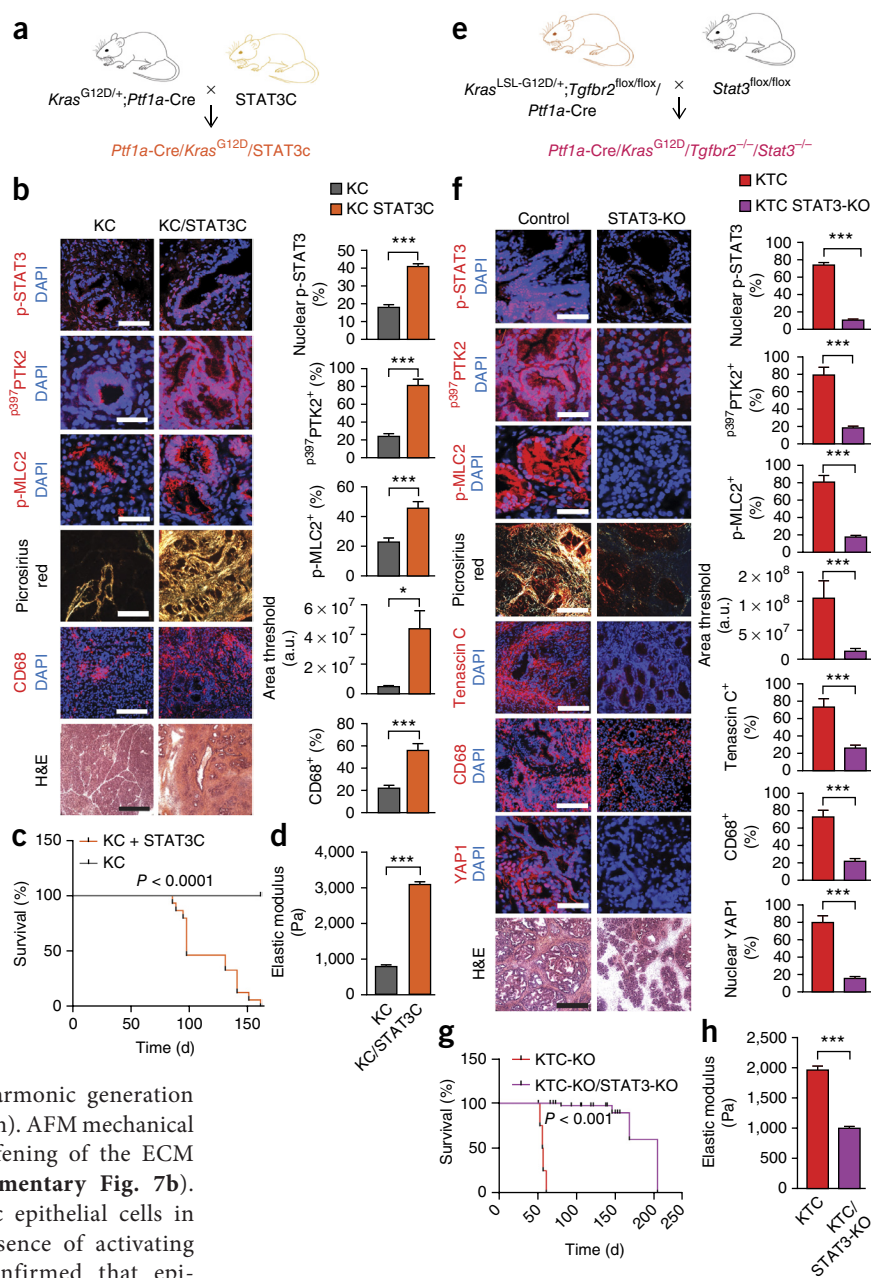
(**Fig. 4a**) and found that the pancreatic epithelium in 5-week-old KC mice expressing β1-V737N (KC/β1-V737N mice) had significantly higher ^{p397}PTK2 ($P \leq 0.001$) and p-MLC2 ($P \leq 0.01$) than KC mice. The amount and distribution of collagen fibers and ECM stiffness were highest in the periductal region (**Fig. 4b**), similarly to our observations in the developing KTC lesions (**Figs. 2a** and **4b**). Consistent with the matricellular-enriched fibrosis observed in both the patient samples lacking p-SMAD and the PDAC lesions in the KTC mice, we detected abundant tenascin C and higher levels of epithelial p-STAT3 in the KC/β1-V737N tumors (**Fig. 4b**). This phenotype was accompanied by an increase in infiltrating CD68+ macrophages (**Fig. 4b**), and FACS characterization of the immune cell population revealed an increase in CD45+CD11b myeloid cells and CD45+Ly6C monocytes (**Supplementary Fig. 9d**). Indeed, cytokine array analysis showed higher levels of proinflammatory factors C5α and IL1 in the pancreas in KC/β1-V737N mice than in KC mice (**Supplementary Fig. 9e**). Chronic pancreatitis was detectable in KC/β1-V737N mice

by 3 months of age (**Fig. 4c**). Alcian blue staining of pancreatic tissue from 3-month-old KC/V737N mice showed that the lesions had progressed to advanced, high-grade PanINs and that these foci were evenly distributed throughout the tissue. By age 5–8 months, 38% of KC/β1-V737N mice developed frank PDACs with accompanying physiological trauma, including loss of body weight (**Fig. 4d** and **Supplementary Fig. 9c**). Orthotopic KTC tumor showed a marked loss of stromal fibrosis and matrix remodeling upon knockdown of *Ptk2* compared to scrambled controls (**Fig. 4e,f**). These results reveal that increasing the cytoskeletal contractility in pancreatic tumor cells drives remodeling and stiffening of the periductal ECM, induces matricellular-enriched fibrosis and promotes pancreatic transformation.

STAT3 induces fibrosis and accelerates PDAC

We next explored the relationship between STAT3 activation, cell contractility and pancreatic matricellular-enriched fibrosis in PDAC. We crossed KC mice to mice expressing one allele of a constitutively active *Stat3* (ref. 49) (**Fig. 5a**). The resulting STAT3C mice contained significantly more p-STAT3-positive cells in the pancreas (**Supplementary Fig. 10a**) ($P \leq 0.001$), and the level of p-STAT3 was further increased after expression of activated KRAS (**Fig. 5b**) compared to wild-type or Ptf1a-Cre and KC mice, respectively. We observed higher numbers of CD45^{+} immune cells ($P \leq 0.001$) and CD68^{+} macrophages ($P \leq 0.05$) within the STAT3C pancreatic tissues (**Supplementary Fig. 10a**); these immune infiltrates further increased with KRAS activation (**Fig. 5b**). Indeed, the pancreatic tissues in constitutively active STAT3 mice crossed to the KC model (KC/Stat3C mice) showed marked pancreatitis that developed into frank PDAC and shortened survival compared to KC mice (**Fig. 5c**). Consistent with a link between STAT3 and ROCK, although tumors were stiffer and p-MLC2 was abundant in the KC/STAT3C mice, p-MLC2 levels were elevated significantly ($P \leq 0.001$) in the pancreatic tissue of STAT3C mice even in the absence of KRAS (**Fig. 5b,d** and

Supplementary Fig. 10a). The pancreas of STAT3C mice contained abundant mature type I collagen (**Supplementary Fig. 10a**) ($P \leq 0.005$) and elevated P397PTK2 throughout (**Supplementary Fig. 10a**) ($P \leq 0.05$). These findings link STAT3 activation and tissue inflammation and suggest that p-STAT3 induces ROCK-dependent ECM remodeling and stiffening to drive fibrosis and elevate mechanosignaling in PDACs.

To establish a causal relationship between STAT3 activation, tissue mechanics and matricellular-enriched fibrosis and PDAC development, we crossed mice expressing KRAS and homozygous for loss of *Tgfbr2* (ref. 21) (*Kras*[LSL-G12D/+]*Tgfbr2*[flox/flox] (KTC-KO) mice), which exhibit an accelerated matricellular-enriched fibrotic phenotype and PDAC development (**Supplementary Fig. 10a–c**), with STAT3-KO mice, which carry a conditional *Stat3* knockout[50] in the pancreatic epithelium (*Stat3*[flox/flox];*Ptf1α*-Cre) to generate KTC-KO/STAT3-KO mice (**Fig. 5e**). Immunostaining confirmed deletion of STAT3 in the pancreatic epithelium (**Fig. 5f**) accompanied by significantly reduced CD68^{+} cell tissue infiltration ($P \leq 0.001$), consistent with decreased inflammation (**Fig. 5f**). Loss of epithelial STAT3 was also accompanied by a significant reduction in epithelial P397PTK2, p-MLC2 and nuclear YAP1 ($P \leq 0.001$) as well as YAP transcriptional activity, as indicated by significantly lower *Ctgf* expression (**Fig. 5f** and **Supplementary Fig. 9b**) ($P \leq 0.05$). Pancreatic tissues lacking epithelial STAT3 showed significant reduction in matricellular-rich fibrosis and ECM stiffness ($P \leq 0.001$) and a significant increase in mouse survival (**Fig. 5f–h**).

Direct links between a matricellular-rich fibrotic phenotype, mechanics and p-STAT3 were confirmed in a cohort of KTC mice treated with the JAK inhibitor ruxolitinib. Ruxolitinib treatment

Figure 6 STAT3 enhances epithelial contractility to induce PDAC fibrosis and aggression. (**a**) Hematoxylin and eosin (H&E) staining (scale bar, 100 μm); second-harmonic generation (SHG) images and quantification of extracellular collagen architecture in the pancreatic tissue around the epithelial ductal region (scale bar, 75 μm); and immunofluorescence images and quantification of tenascin C, fibronectin, collagen XII α1 (collagen 12), p-STAT3, YAP1 and DAPI (scale bars, 75 μm (main) and 10 μm (inset)) in PDAC tumors from patients with a median short survival of 11–289 d ($n = 29$) and median long survival of 1,090–3,298 d ($n = 28$). (**b**) H&E staining (scale bar, 100 μm); SHG images and quantification of periductal collagen (scale bar, 75 μm); and immunofluorescence and quantification of tenascin C, fibronectin, collagen 12, p-STAT3, YAP1 and DAPI (scale bars, 75 μm) in PDAC tumors from patients with wild-type (WT) SMAD4 ($n = 10$) or mutant (mut) SMAD4 ($n = 10$). Results are presented as mean ± s.e.m. *$P < 0.05$; **$P < 0.01$; ***$P < 0.001$; ****$P < 0.0001$, unpaired two-sided Student's *t*-test.
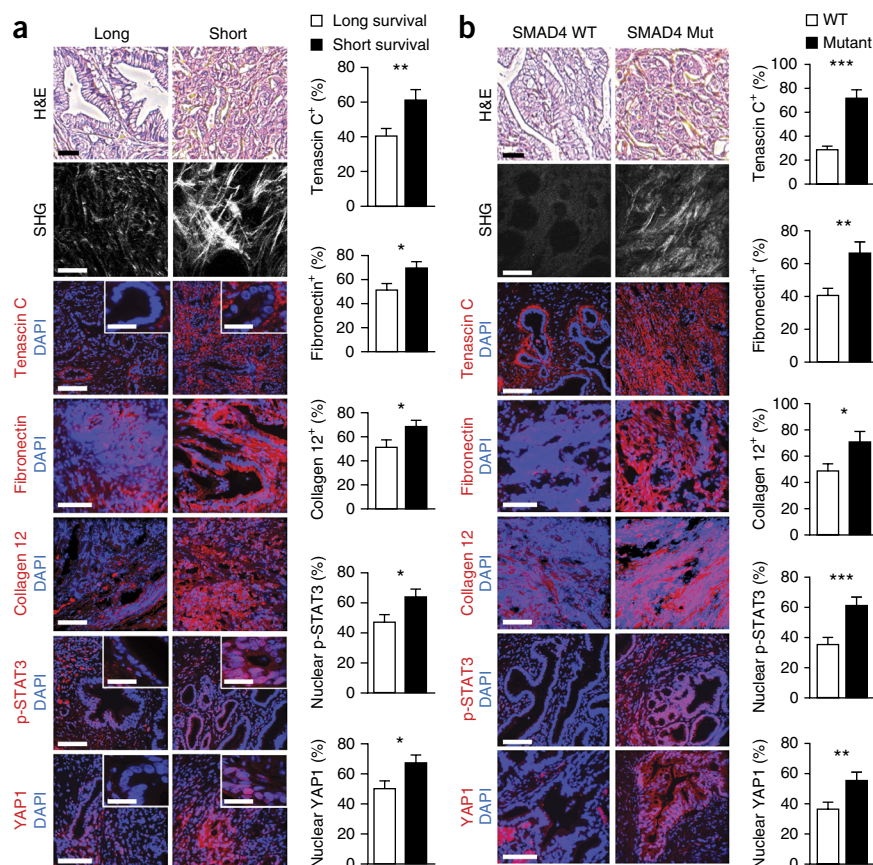
inhibited p-STAT3 activity and significantly reduced ^{P397}PTK2, p-MLC2, collagen fibrillogenesis, matricellular matrix enrichment and ECM stiffening (**Supplementary Fig. 11c,d**) ($P \le 0.01$–0.001) as well as YAP activation (data not shown). Moreover, in the absence of JAK-driven matricellular-rich fibrosis, mechanosignaling, STAT3-dependent inflammation and PDAC development were significantly reduced (**Supplementary Fig. 11c,e**) ($P \le 0.01$–0.001).

We investigated the clinical relevance of STAT3 activation in matricellular-enriched fibrosis and PDAC progression, and found elevated levels of tenascin C, fibronectin and collagen 12 ($P \le 0.05$), high nuclear YAP1 ($P \le 0.05$) (**Fig. 6a**) and elevated SOX2, vimentin ($P \le 0.01$; **Supplementary Fig. 12a**) and p-STAT3 (**Fig. 6a**; $P \le 0.05$) in the mesenchymal-like, vimentin-positive PDAC biopsies excised from patients with shorter median survival. The PDAC tissue with confirmed SMAD4 mutations also had elevated levels of epithelial p-STAT3 ($P \le 0.001$), tenascin C ($P \le 0.001$), fibronectin ($P \le 0.01$) and collagen type XII α1 ($P \le 0.05$) (**Fig. 6b**). The epithelium in the PDAC tumors with mutant SMAD4 was more mechanically activated, as evidenced by a significant increase in nuclear YAP1 ($P \le 0.01$). Moreover, the samples with SMAD4 mutations had significantly higher nuclear SOX2 ($P \le 0.01$) and contained significantly more vimentin ($P \le 0.001$), which is consistent with a quasi-mesenchymal phenotype that typically has an aggressive disease pathology (**Supplementary Fig. 12b**).

DISCUSSION

Using clinical specimens and experimental mouse models, we identified a unique, highly rigid, matricellular-stromal phenotype linked specifically to a PDAC genotype that results in reduced epithelial TGF-β signaling and elevated tumor cell contractility. Our data suggest that the genetically induced tumor cell tension differentially 'tunes' the composition and mechanics of the periductal stroma in PDACs, regardless of the bulk stromal phenotype, to promote tumor progression and aggression by engaging mechanosignaling pathways linked to integrins and YAP. The findings are consistent with the mathematical predictions identifying two distinct stromal phenotypes termed 'normal' and 'activated' in PDAC subtypes of increasing aggression[24]. Our findings provide the first direct evidence that tumor genotype *per se* can calibrate tumor cell contractility to modulate the fibrotic phenotype of the tissue and modify the pathology of the cancer. Our data further suggest that bulk collagen content is a poor surrogate for the multifaceted contributions of PDAC fibrosis to cancer aggression and advocate imaging approaches to visualize differential distribution of the stroma such as MR imaging and elastography[51].

PDAC-associated fibrosis has been viewed as a constraint that directly compromises lymphatic drainage and impedes neovascularization and indirectly increases interstitial fluid pressure to disrupt blood vessel integrity and induce hypoxia[1]. This physical barrier compromises drug delivery, reduces immune cell accessibility and promotes disease aggression and therapy resistance, underscoring the critical importance of tissue mechanics to tumor biology[4,12,52]. Notably, our data show that the fibrosis is not merely a passive physical restraint. Rather, the elevated tissue mechanics directly activate key pathways such as integrin-dependent signaling and YAP to promote tumor progression and aggression[10–12]. To this end, our clinical findings revealed that poorly differentiated PDACs and the PDACs with impaired TGF-β signaling were the most mechanically activated and expressed elevated YAP1 and SOX2, which are transcriptional regulators that have been implicated in tumor aggression and

epithelial-to-mesenchymal transition[53–56]. Indeed, these same YAP1 and SOX2-expressing tumors expressed markers of a mesenchymal-like phenotype including vimentin, fibronectin and tenascin C[57–59] (**Fig. 6b**). Our findings thus imply that the more aggressive phenotype of PDACs with a quasi-mesenchymal phenotype may be linked to their altered mechanobehavior. Moreover, given that YAP signaling can drive KRAS-independent PDAC growth and survival, our observations indicate that fibrotic PDAC tumors may naturally evolve toward KRAS independence and that this phenotype will be potentiated by specific tumor genotypes that increase tissue fibrosis including loss of TGF-β signaling. Our data thereby present a plausible reason for the mixed responses of PDAC cancer patients to antistromal therapies, and suggest that PTK2 and JAK inhibitors, which target both stromal- and epithelial-driven fibrosis and reduced YAP1 and tenascin induction in our studies, may comprise more efficacious therapeutic options.

METHODS

Methods and any associated references are available in the online version of the paper.

Note: Any Supplementary Information and Source Data files are available in the online version of the paper.

AUTHOR CONTRIBUTIONS
V.M.W. conceived the project, and designed and directed all of the studies with input from all authors. H.L. conducted transgenic mouse experiments and treatments. H.L. performed histology, immunofluorescence and image analysis on mice and human samples, conducted experiments with the PA hydrogels, and performed 3D collagen and soft agar assays, cytokine arrays, immunoblotting and related analyses. H.L. and Y.A.M. performed AFM imaging and analysis. Y.A.M. performed TFM and two-photon imaging and analysis. H.L. and M.W.P. conducted orthotopic xenograft experiments. M.W.P. performed RT-PCR and bioinformatics. S.V.N. and M.W.P. performed flow sorting. J.N.L. designed and constructed expression constructs and the V737N transgenic mouse. E.A.C. and G.E.K. aided with pathological pancreatic cancer scoring of transgenic mice and human samples. J.S.J. and E.A.C. collected human samples from short- and long-survival patients and aided in the interpretation of the data. C.A.I.-D. and L.D.W. collected human samples from wild-type and mutant SMAD4 patients and aided in the interpretation of the data. R.K., V.S.L., M.H. and N.R. provided KPC pancreatic tissues. V.P. provided *Stat3*$^{flox/flox}$ and constitutively active STAT3C transgenic mice. A.S.B., R.C.H. and K.H. performed LC-MS-MS and LC-SRM proteomic analysis. D.D.S. provided Ptk2 inhibitor PND-1186. H.L.M. designed and provided KTC transgenic mouse, provided KC mice and aided in interpretation of data. V.M.W., H.L., Y.A.M., J.K.M. and M.W.P. wrote the manuscript with input from all authors.

1. Chauhan, V.P. *et al*. Angiotensin inhibition enhances drug delivery and potentiates chemotherapy by decompressing tumour blood vessels. *Nat. Commun.* **4**, 2516 (2013).
2. Swartz, M.A. & Lund, A.W. Lymphatic and interstitial flow in the tumour microenvironment: linking mechanobiology with immunity. *Nat. Rev. Cancer* **12**, 210–219 (2012).
3. Yu, M. & Tannock, I.F. Targeting tumor architecture to favor drug penetration: a new weapon to combat chemoresistance in pancreatic cancer? *Cancer Cell* **21**, 327–329 (2012).

4. Provenzano, P.P. & Hingorani, S.R. Hyaluronan, fluid pressure, and stromal resistance in pancreas cancer. *Br. J. Cancer* **108**, 1–8 (2013).
5. Olive, K.P. *et al.* Inhibition of Hedgehog signaling enhances delivery of chemotherapy in a mouse model of pancreatic cancer. *Science* **324**, 1457–1461 (2009).
6. Provenzano, P.P. *et al.* Enzymatic targeting of the stroma ablates physical barriers to treatment of pancreatic ductal adenocarcinoma. *Cancer Cell* **21**, 418–429 (2012).
7. Rosow, D.E. *et al.* Sonic Hedgehog in pancreatic cancer: from bench to bedside, then back to the bench. *Surgery* **152** (suppl. 1), S19–S32 (2012).
8. Özdemir, B.C. *et al.* Depletion of carcinoma-associated fibroblasts and fibrosis induces immunosuppression and accelerates pancreas cancer with reduced survival. *Cancer Cell* **25**, 719–734 (2014).
9. Rhim, A.D. *et al.* Stromal elements act to restrain, rather than support, pancreatic ductal adenocarcinoma. *Cancer Cell* **25**, 735–747 (2014).
10. Jain, R.K., Martin, J.D. & Stylianopoulos, T. The role of mechanical forces in tumor growth and therapy. *Annu. Rev. Biomed. Eng.* **16**, 321–346 (2014).
11. Neesse, A. *et al.* Stromal biology and therapy in pancreatic cancer. *Gut* **60**, 861–868 (2011).
12. Stromnes, I.M., DelGiorno, K.E., Greenberg, P.D. & Hingorani, S.R. Stromal reengineering to treat pancreas cancer. *Carcinogenesis* **35**, 1451–1460 (2014).
13. Cheung, K.J., Gabrielson, E., Werb, Z. & Ewald, A.J. Collective invasion in breast cancer requires a conserved basal epithelial program. *Cell* **155**, 1639–1651 (2013).
14. Hoadley, K.A. *et al.* Multiplatform analysis of 12 cancer types reveals molecular classification within and across tissues of origin. *Cell* **158**, 929–944 (2014).
15. Cancer Genome Atlas Research Network. Comprehensive molecular profiling of lung adenocarcinoma. *Nature* **511**, 543–550 (2014).
16. Sugimoto, H., Mundel, T.M., Kieran, M.W. & Kalluri, R. Identification of fibroblast heterogeneity in the tumor microenvironment. *Cancer Biol. Ther.* **5**, 1640–1646 (2006).
17. Wang, Y., You, M. & Wang, Y. Alternative splicing of the K-ras gene in mouse tissues and cell lines. *Exp. Lung Res.* **27**, 255–267 (2001).
18. Paszek, M.J. *et al.* Tensional homeostasis and the malignant phenotype. *Cancer Cell* **8**, 241–254 (2005).
19. Samuel, M.S. *et al.* Actomyosin-mediated cellular tension drives increased tissue stiffness and β-catenin activation to induce epidermal hyperplasia and tumor growth. *Cancer Cell* **19**, 776–791 (2011).
20. Iacobuzio-Donahue, C.A. *et al.* DPC4 gene status of the primary carcinoma correlates with patterns of failure in patients with pancreatic cancer. *J. Clin. Oncol.* **27**, 1806–1813 (2009).
21. Whittle, M.C. *et al.* RUNX3 controls a metastatic switch in pancreatic ductal adenocarcinoma. *Cell* **161**, 1345–1360 (2015).
22. Ijichi, H. *et al.* Aggressive pancreatic ductal adenocarcinoma in mice caused by pancreas-specific blockade of transforming growth factor-β signaling in cooperation with active Kras expression. *Genes Dev.* **20**, 3147–3160 (2006).
23. Collisson, E.A. *et al.* Subtypes of pancreatic ductal adenocarcinoma and their differing responses to therapy. *Nat. Med.* **17**, 500–503 (2011).
24. Moffitt, R.A. *et al.* Virtual microdissection identifies distinct tumor- and stroma-specific subtypes of pancreatic ductal adenocarcinoma. *Nat. Genet.* **47**, 1168–1178 (2015).
25. Kabashima, A. *et al.* Side population of pancreatic cancer cells predominates in TGF-β-mediated epithelial to mesenchymal transition and invasion. *Int. J. Cancer* **124**, 2771–2779 (2009).
26. Dangi-Garimella, S. *et al.* Three-dimensional collagen I promotes gemcitabine resistance in pancreatic cancer through MT1-MMP-mediated expression of HMGA2. *Cancer Res.* **71**, 1019–1028 (2011).
27. Erkan, M. *et al.* The activated stroma index is a novel and independent prognostic marker in pancreatic ductal adenocarcinoma. *Clin. Gastroenterol. Hepatol.* **6**, 1155–1161 (2008).
28. Sinn, M. *et al.* α-smooth muscle actin expression and desmoplastic stromal reaction in pancreatic cancer: results from the CONKO-001 study. *Br. J. Cancer* **111**, 1917–1923 (2014).
29. Bever, K.M. *et al.* The prognostic value of stroma in pancreatic cancer in patients receiving adjuvant therapy. *HPB* **17**, 292–298 (2015).
30. Wang, W.Q. *et al.* Intratumoral α-SMA enhances the prognostic potency of CD34 associated with maintenance of microvessel integrity in hepatocellular carcinoma and pancreatic cancer. *PLoS One* **8**, e71189 (2013).
31. Rath, N. & Olson, M.F. Rho-associated kinases in tumorigenesis: re-considering ROCK inhibition for cancer therapy. *EMBO Rep.* **13**, 900–908 (2012).
32. Schultz, N.A. *et al.* MicroRNA expression profiles associated with pancreatic adenocarcinoma and ampullary adenocarcinoma. *Mod. Pathol.* **25**, 1609–1622 (2012).
33. Pérez-Mancera, P.A., Guerra, C., Barbacid, M. & Tuveson, D.A. What we have learned about pancreatic cancer from mouse models. *Gastroenterology* **142**, 1079–1092 (2012).
34. Macias, M.J., Martin-Malpartida, P. & Massagué, J. Structural determinants of Smad function in TGF-β signaling. *Trends Biochem. Sci.* **40**, 296–308 (2015).
35. Shi, Y. & Massagué, J. Mechanisms of TGF-β signaling from cell membrane to the nucleus. *Cell* **113**, 685–700 (2003).
36. Yachida, S. *et al.* Clinical significance of the genetic landscape of pancreatic cancer and implications for identification of potential long-term survivors. *Clin. Cancer Res.* **18**, 6339–6347 (2012).
37. Hingorani, S.R. *et al.* Preinvasive and invasive ductal pancreatic cancer and its early detection in the mouse. *Cancer Cell* **4**, 437–450 (2003).
38. Hingorani, S.R. *et al.* Trp53^{R172H} and Kras^{G12D} cooperate to promote chromosomal instability and widely metastatic pancreatic ductal adenocarcinoma in mice. *Cancer Cell* **7**, 469–483 (2005).
39. Dupont, S. *et al.* Role of YAP/TAZ in mechanotransduction. *Nature* **474**, 179–183 (2011).
40. Blackford, A. *et al.* SMAD4 gene mutations are associated with poor prognosis in pancreatic cancer. *Clin. Cancer Res.* **15**, 4674–4679 (2009).
41. Sanz-Moreno, V. *et al.* ROCK and JAK1 signaling cooperate to control actomyosin contractility in tumor cells and stroma. *Cancer Cell* **20**, 229–245 (2011).
42. Fukuda, A. *et al.* Stat3 and MMP7 contribute to pancreatic ductal adenocarcinoma initiation and progression. *Cancer Cell* **19**, 441–455 (2011).
43. Lesina, M. *et al.* Stat3/Socs3 activation by IL-6 transsignaling promotes progression of pancreatic intraepithelial neoplasia and development of pancreatic cancer. *Cancer Cell* **19**, 456–469 (2011).
44. Nagathihalli, N.S. *et al.* Signal transducer and activator of transcription 3, mediated remodeling of the tumor microenvironment results in enhanced tumor drug delivery in a mouse model of pancreatic cancer. *Gastroenterology* **149**, 1932–1943 (2015).
45. Ijichi, H. *et al.* Inhibiting Cxcr2 disrupts tumor-stromal interactions and improves survival in a mouse model of pancreatic ductal adenocarcinoma. *J. Clin. Invest.* **121**, 4106–4117 (2011).
46. Schrader, J. *et al.* Matrix stiffness modulates proliferation, chemotherapeutic response, and dormancy in hepatocellular carcinoma cells. *Hepatology* **53**, 1192–1205 (2011).
47. Mouw, J.K. *et al.* Tissue mechanics modulate microRNA-dependent PTEN expression to regulate malignant progression. *Nat. Med.* **20**, 360–367 (2014).
48. Li, R. *et al.* Activation of integrin αIIbβ3 by modulation of transmembrane helix associations. *Science* **300**, 795–798 (2003).
49. Barbieri, I. *et al.* Constitutively active Stat3 enhances neu-mediated migration and metastasis in mammary tumors via upregulation of Cten. *Cancer Res.* **70**, 2558–2567 (2010).
50. Alonzi, T. *et al.* Essential role of STAT3 in the control of the acute-phase response as revealed by inducible gene inactivation in the liver. *Mol. Cell. Biol.* **21**, 1621–1632 (2001).
51. Luna, A. *et al.* Multiparametric MR imaging in abdominal malignancies. *Magn. Reson. Imaging Clin. N. Am.* **24**, 157–186 (2016).
52. Chauhan, V.P. *et al.* Compression of pancreatic tumor blood vessels by hyaluronan is caused by solid stress and not interstitial fluid pressure. *Cancer Cell* **26**, 14–15 (2014).
53. Herreros-Villanueva, M. *et al.* SOX2 promotes dedifferentiation and imparts stem cell-like features to pancreatic cancer cells. *Oncogenesis* **2**, e61 (2013).
54. Shao, D.D. *et al.* KRAS and YAP1 converge to regulate EMT and tumor survival. *Cell* **158**, 171–184 (2014).
55. Jiang, J. *et al.* MiR-1181 inhibits stem cell-like phenotypes and suppresses SOX2 and STAT3 in human pancreatic cancer. *Cancer Lett.* **356**2 Pt B, 962–970 (2015).
56. Yimlamai, D. *et al.* Hippo pathway activity influences liver cell fate. *Cell* **157**, 1324–1338 (2014).
57. Kohler, I. *et al.* Detailed analysis of epithelial-mesenchymal transition and tumor budding identifies predictors of long-term survival in pancreatic ductal adenocarcinoma. *J. Gastroenterol. Hepatol.* **30** (suppl. 1), 78–84 (2015).
58. Paron, I. *et al.* Tenascin-C enhances pancreatic cancer cell growth and motility and affects cell adhesion through activation of the integrin pathway. *PLoS ONE* **6**, e21684 (2011).
59. Esposito, I. *et al.* Tenascin C and annexin II expression in the process of pancreatic carcinogenesis. *J. Pathol.* **208**, 673–685 (2006).

ONLINE METHODS

Human samples. Formalin-fixed, paraffin-embedded human PDAC tissue sections, lacking any patient-identifying information, were commercially purchased from US Biomax (PA961a) or obtained from a cohort of patients on the basis of long and short survival. For noncommercial human samples, the study was approved by Regional Scientific Ethics Committee of the Capital Region of Denmark (protocol H-KA-20060181) in Region Hovedstaden, Denmark. The use of control materials was approved by the Ethical Committees in Bergen, Norway, and in Heidelberg, Germany[32]. Informed consent was obtained from human subjects. Snap-frozen human PDAC tissues were collected from autopsy participants with stage IV disease in association with the Gastrointestinal Cancer Rapid Medical Donation Program (GICRMDP), and the study was approved by the Johns Hopkins Institutional Review Board[36] (protocol 36610).

Mouse studies. All mice were maintained in accordance with University of California Institutional Animal Care and Use Committee guidelines under protocol number AN105326-01D. Transgenic mouse strains $Kras^{LSL-G12D/+}$;$Ptf1a$-Cre (KC)[37]; $Kras^{LSL-G12D/+}$;$Tgfbr2^{flox/wt}$ or $Tgfbr2^{flox/flox}$;$Ptf1a$-Cre (KTC)[22]; $Kras^{LSL-G12D/+}$;$Tp53^{R172H/+}$; $Pdx1$-Cre (KPC)[38], LSL-β1V737N[47], $Stat3^{flox/flox}$ (ref. 51) and constitutively active STAT3C (ref. 49) were described previously. Mice were interbred and maintained in mixed background. Age-matched littermates not expressing Cre as well as $Ptf1a$-Cre and $Pdx1$-Cre mice were used as controls; mixed sexes were used for all experiments except xenograft studies, which included only female mice.

For PTK2 (FAK) inhibition studies, $Ptf1a$-Cre/β1-V737N mice were treated with FAK inhibitor PND-1186 at 0.5 mg/ml in 5% sucrose in the drinking water, control mice were provided 5% sucrose as drinking water ($n = 5$ per group). Treatment started at 3 weeks of age. At this time point, mice exhibit pancreatitis and fibrosis at 3 weeks of age and mice were killed after 3 weeks owing to animal protocol guidelines. For JAK inhibition, KTC mice were treated with JAK inhibitor ruxolitinib twice daily by oral gavage at 60 mg per kg body weight (mg/kg) in 0.5% methylcellulose in water. Control mice were provided 0.5% methylcellulose in water ($n = 5$ per group). Treatment started at 3 weeks and mice were killed after 3 weeks.

For orthotopic xenografts, 5×10^5 firefly-luciferase-mApple-expressing cells in Matrigel (BD Biosciences) were injected into the pancreas of 8-week-old nude mice (Simonsen laboratory) ($n = 5$ per group), and tumor growth was monitored by weekly bioluminescence imaging. Mice were sacrificed at 2 weeks after the cell injection per animal protocol. Female mice were used in the xenograft studies.

For bioluminescence imaging, animals were injected intraperitoneally with 3 mg of D-luciferin and imaged using IVIS spectrum imaging system. Living Image 4.3 was used for analysis of the images after acquisition.

For all animal studies, animals were randomly distributed among different conditions by the investigator as the animals did not show any size or appearance differences at the onset of the experiments. No animals were excluded, and the investigator was not blinded to group allocation during the experiment.

Histology. Paraffin-embedded or fresh-frozen pancreatic tissues were analyzed by hematoxylin and eosin (H&E), picrosirius red, Masson's trichrome or Alcian blue according to the manufacturer's instructions. For mouse and clinical studies, staining intensity of tissue sections was scored by a pathologist blinded to mouse genotype.

LC-MS-MS and LC-SRM proteomic analysis. Proteomic analysis was performed in triplicate on 5 mg of fresh-frozen KC, KPC, and KTC pancreatic tissues as previously described[60]. Briefly, tissues were milled in liquid nitrogen followed by sequential extraction of cellular proteins, soluble ECM proteins, and insoluble ECM proteins. Tryptic digests of all fractions were analyzed by liquid chromatography-select reaction monitoring (LC-SRM) mass spectrometry (MS). Stable isotope labeled (SIL) peptides were used for absolute quantification of ECM proteins by LC-SRM.

Atomic force microscopy measurements. Atomic force microscopy (AFM) and analysis were performed as previously described[61]. Frozen tissue blocks were cut into 20-μm-thick sections. Prior to AFM measurement, each section was immersed in PBS and thawed at room temperature. The samples were maintained in proteinase inhibitor in PBS (protease inhibitor cocktail, Roche 14 Diagnostics, 11836170001) supplemented with propidium iodide (Sigma P4170, 20 μg/ml) during the AFM session. Five samples for each group were used for AFM quantification of Young's elastic modulus of the cancer-associated stroma. AFM indentations were performed using an MFP3D-BIO inverted optical AFM (Asylum Research) mounted on a Nikon TE2000-U inverted fluorescent microscope as previously described[61]. Briefly, we used silicon nitride cantilevers with spring constant of 0.06 N/m with borosilicate glass spherical tip with 5 μm in diameter (Novascan Tech). The cantilever was calibrated using the thermal oscillation method before each experiment. Samples were indented at a 20 μm/s loading rate, with a maximum force of 2 nN. Five AFM force maps were typically obtained on each sample, each map as a 10×10 μm raster series of indentations using the FMAP function of the IGOR PRO build supplied by Asylum Research. The Hertz model was used to determine the elastic properties of the tissue (E1). Tissue samples were assumed to be incompressible and a Poisson's ratio of 0.5 was used in the calculation of the Young's elastic modulus.

Two-photon second-harmonics microscopy and image analysis. Two-photon imaging of pancreatic tissues and collagen gels was performed and quantified as previously described[62]. For two-photon imaging, we used custom resonant-scanning instruments based on published designs containing a 5-PMT array (Hamamatsu, C7950) operating at video rate[63]. The setup was used with two-channel simultaneous video rate acquisition via two PMT detectors and an excitation laser (2W MaiTai Ti-Sapphire laser, 710–920 nm excitation range). Second-harmonics imaging was carried out on a Prairie Technology Ultima System attached to an Olympus BX-51 fixed stage microscope equipped with a 25× (numerical aperture (NA) 1.05) water-immersion objective. Unfixed, hydrated samples were exposed to polarized laser light at a wavelength of 830 nm and emitted light was separated with a filter set (short-pass filter, 720 nm; dichroic mirror, 495 nm; band-pass filter, 475/40 nm). Images of x and y planes of 284 by 284 μm at a resolution of 0.656 μm/pixel were captured using Micro-Manager Open Source Microscopy Software (Micro-Manager). Quantification of collagen fibers was achieved by setting a minimal threshold in the second-harmonic signal. The threshold was maintained for all images across all conditions. The area of regions that was covered by the minimal threshold was calculated, and three images per sample were averaged together (ImageJ, Image Processing and Analysis in Java). Collagen fiber diameter data were visualized and analyzed using Imaris (Bitplane AG) and MATLAB (MathWorks).

Cell culture and establishment of primary pancreatic cell lines. Establishment of primary pancreatic tumor cells was performed as described previously[64]. Cells were maintained in RPMI-1640 medium containing 10% FBS (Clontech). All experiments were performed within eight passages to avoid possible gross genomic changes during long-term *in vitro* culture. Cells were verified by epithelial morphology in two dimensions (2D), expression of the epithelial marker cytokeratin 19 and the ability to form tumors *in vivo*. Cells were tested for mycoplasma contamination using a commercially available kit (PCR-Mycoplasma Test Kit I/C, Promokine PK-CA91-1024) according to manufacturer's manual at the onset of the study (test was negative) and exhibited no contamination signs after the test. Derivative cells were transduced *in vitro* with a lentiviral vector encoding firefly Luciferase and mApple fluorescent protein for combined bioluminescent imaging and flow sorting. To ensure that all cell lines expressed similar levels of luciferase, mApple-expressing cells were flow sorted before injection into animals.

Soft-agar assay. Anchorage-independent growth was assessed using a soft-agar assay[65]. In brief, 25,000 cells in 1.5 ml 0.35% agarose containing 1× growth medium were overlaid with 1.5 ml 0.5% agarose containing 1× growth medium, and colonies larger than 30 μm in diameter were scored positive after 14 d.

Lentivirus-mediated shRNA knockdown. Lentiviral shRNA targeting ROCK1, ROCK2 and FAK and nontargeting shRNA control were cloned in the pLKO vector. The clone IDs for shRNA are as follows: sh-ROCK1 (TRCN0000022903),

sh-ROCK2 (TRCN0000022922), sh-FAK (TRCN0000023485) and eEGFP as a nonspecific control cloned into the lentiviral pLKO.1 puro vector (Sigma-Aldrich).

Preparation of luciferase-mApple-virus-infected cells. Lentivirus infection was performed with pLKO EEF1α mApple luc2 lentiviral vector for combined flow sorting and *in vivo* imaging. This was constructed from the pLKO.1 puro vector (Sigma-Aldrich SHC001) by inserting an in-frame fusion of mApple with the human codon optimized firefly luciferase gene from pGL4.10[luc2] (Promega) and placing this under control of the human EEF1α promoter. This cassette, followed by a WPRE element, was inserted in place of the U6-cppt-mPGK-puro elements in pLKO.1 puro (from ClaI to KpnI sites).

Quantitative real-time PCR. RNA was extracted by TRIzol-chloroform isolation followed by Ambion mirVana kit (Thermo Fisher Scientific, AM1560). Total RNA was reverse-transcribed using random primers (Amersham Biosciences), and β-actin primers were used to control for cDNA concentration in a separate PCR reactions for each sample. LightCycler Fast Start DNA Master SYBR Green Mix (Roche) was added to each PCR reaction along with cDNA and 1 pmol primer in a total volume of 10 μl. Quantitative PCR (qPCR) was performed on an Eppendorf RealPlex2 Mastercycler using the real-time primers provided, according to the manufacturer's instructions. C_t values were converted to fold expression changes ($2^{-\Delta\Delta Ct}$ values) following normalization to β-actin. Primer sequences were as follows: *CTGF* forward, 5′-GTGAGTCCTTCCAAAGCAGC-3′, reverse, 5′-TAGTTGGGTCTGGGCCAAAT-3′; *Actb* forward, 5′-GTGGGCC GCCCTAGGCACCA-3′; reverse, 5′-CGGTTGGCCTTAGGGTTCAGGG-3′.

Traction-force microscopy. Traction of pancreatic cells was measured as previously described[18,66]. Images of cells on PA gels containing fluorescent beads were collected before and after trypsinization using a Nikon Inverted Eclipse TE300 microscope and a Photometric Cool Snap HQ camera (Roper Scientific). TFMs were calculated on the basis of differences in bead displacement induced by substrate deformation and relaxation using a software analysis program.

Three-dimensional collagen-contraction assay. Collagen contraction assay was performed as previously described[41]. Briefly, collagen I solution was prepared by neutralizing acid-solubilized rat tail collagen I (BD Bioscience) with 1 N NaOH and DMEM buffer. Neutralized collagen was added at 300 μl/well in 24-well plates and polymerized at 37 °C. Cells were seeded on top of collagen and allowed to adhere overnight. Collagen gel area was quantified using NIH ImageJ analysis software.

Polyacrylamide substrates. Basement-membrane-conjugated polyacrylamide hydrogels were prepared as previously described[67] with one modification: *n*-succinimidyl acrylamidohexanoic acid crosslinker was conjugated to polyacrylamide substrates using 0.01% bisacrylamide, 0.025% Irgacure 2959 0.002% di(trimethylolpropane) tetracrylate (Sigma) and 0.01% *n*-succinimidyl acrylamidohexanoic acid.

Cytokine antibody array. Proteins from pancreatic cells or tissues were screened using the Mouse Cytokine Antibody Array A (R&D ARY006) according to the manufacturer's instructions. In brief, conditioned medium or protein lysate was collected and subjected to the antibody array incubation. The amount of conditioned medium used was normalized by the cell number. The membranes were washed and incubated with primary biotin-conjugated antibody and then incubated with horseradish-peroxidase-conjugated streptavidin, and the protein spots were detected using the ECL western blotting detection reagents (GE Healthcare) according to the manufacturer's instructions. The spot density was quantified and compared between different conditions.

Tissue processing and immunostaining. Fresh tumors were harvested and embedded in O.C.T. medium (TissueTek) before freezing in liquid nitrogen. Frozen sections 5 μm thick were fixed in PFA for 15 min. Paraffin-embedded harvested tumors were formalin fixed before paraffin embedding. Sections 5 μm thick were deparaffinized, rehydrated and boiled for 1 h in 10 mM citrate buffer at pH 6.0. For all stains, the tissue sections were blocked with 5% NGS,

0.3% Triton X-100 in PBS for 60 min at room temperature. Sections were then incubated with primary antibodies overnight at 4 °C followed by incubation with fluorochrome-conjugated secondary antibodies for 1 h at room temperature. 1% BSA, 0.3% Triton X-100 in PBS was used to dilute primary and secondary antibodies. DAPI was used to stain cell nuclei. All stainings were quantified using NIH ImageJ analysis software with the same threshold for each stain; positivity was analyzed in five visual fields for each sample, and results were expressed as percentage staining per visual field.

Antibodies and reagents. Antibodies were as follows: α-SMA (Sigma-Aldrich C6198, 1:1,000), GLi-1 (Thermo Scientific PA5-32206, 1:500), tenascin C (Abcam AB108930, 1:500), fibronectin (Abcam AB2413, 1:500), Collagen 12A1 (Santa Cruz Biotechnology E-15 sc-68449, 1:200), SOX2 (Abcam ab97959, 1:500), Vimentin (Cell Signaling 5741S, 1:200), FAP (Abcam AB53066, 1:500), Collagen III (Abcam AB7778, 1:500), YAP (Cell signaling 4912, 1:200), β1-integrin (EMD Millipore MABT409, 1:500), pY397-FAK (^{P397}PTK2) (Invitrogen 44625, 1:200), total FAK (BD Biosciences 610088, 1:1,000), ROCK1 (Cell Signaling C8F7, 1:1,000), ROCK2 (Cell Signaling D1B1, 1:1,000), p-MLC2 (Cell Signaling 3671, 1:200), p-MyPT1 (Millipore ABS45, 1:200), p-STAT3 (Cell Signaling 9145, 1:200), p-SMAD2/3 (Cell Signaling 8828, 1:200), total STAT3 (Cell Signaling 9132, 1:1,000), GAPDH (Cell Signaling 2118, 1:5,000), CD45 (BD Biosciences 550539, 1:200), CD68 (Thermo Scientific Ab-3, 1:200), Alexa-Fluor-conjugated goat secondary anti-mouse IgG and anti-rabbit IgG antibodies (Invitrogen A11012, 1:1,000 and A11005, 1:1,000) and HRP-conjugated rabbit secondary antibody (GE Healthcare Life Sciences NA934VS, 1:5,000).

Immunoblotting. Immunoblotting analyses were performed as previously described[68]. In brief, equal amounts of cell protein lysate (Laemmli) were separated on reducing SDS-PAGE gels, transferred to nitrocellulose membranes, and probed with primary antibody. Bands were visualized and quantified using a PXI 6 Touch (Syngene), in conjunction with HRP-conjugated secondary antibodies and ECL (Amersham Pharmacia).

Flow sorting. Weighed tumors were minced and digested in a mixture of 1 mg/ml of collagenase P (Roche 11213857001), 0.1 mg/ml collagenase I (Sigma, C0130), 0.1 mg/ml dispase II (Roche, 04942078001) and DNase (5 MU/ml, Calbiochem, 260913) in DMEM at 37 °C for 30 min. The tissue lysate was filtered through a 40-μm mesh before immunostaining. The resulting single-cell suspension was stained with fixable viability dye eFluor 780, anti-CD45-APC-Cy7 (103115, 1:200), anti-CD11b-FITC (101205, 1:100) and anti-Ly6/C-PE (128007, 1:100) (all from BioLegend). The percentage of positive cells were analyzed by FlowJo and gated on CD45 positivity. Unstained, live/dead only, and single stain served as controls. Doublets were gated out using forward-scatter width/height and side-scatter width/height event characteristics.

Bioinformatics. Patient expression data were pulled from a publicly available data set (GEO GSE21501). After baseline normalization, expression values for Col1a2, Col2a1, and Col4a1 were used to create a median centroid value representing an average collagen-expression score for each patient. These values were then divided into high and low expression on the basis of median centroid value for the patient set and graphed as survival of each group over time. Kaplan–Meier survival curves were analyzed by Mantel–Cox log–rank analysis.

Statistical analysis. All quantitative results were assessed by unpaired Student's *t*-test after confirming that the data met appropriate assumptions (normality, homogenous variance, and independent sampling), nonparametric Wilcoxon–Mann–Whitney exact test (using the normal approximation for the *U*-score), or the Kolmogorov–Smirnov distribution test, all two-tailed. For all *in vitro* experiments, three technical replicates were analyzed for each experiment, and results are presented as the mean ± s.e.m. of three biological replicates. For all *in vivo* experiments, five biological replicates were analyzed for each condition, and results are presented as the mean ± s.e.m. Subsequent statistical analysis was performed with either unpaired two-sided student *t*-tests or one-way ANOVA with Tukey's method for multiple comparisons. For survival analysis, the log–rank (Mantel–Cox) test was used. Prism software was used to conduct the statistical analysis of all data. $P < 0.05$ was considered to be significant.

$*P < 0.05$, $**P < 0.01$, $***P < 0.001$, $****P < 0.0001$. Sample size estimation was initially performed using the Mann–Whitney test[69] as a guide and taking into consideration previous experience with assay sensitivity, tissue collection and the different animal strains used. For the listed sample size per group at each time point, the numbers provide a minimum of 85% power to detect an effect size of 2.5 (tumor size, stiffness, gene expression, protein expression) with two-sided type I error = 5% ($P \leq 0.05$). The effect size is defined (where applicable). For mouse and clinical studies, staining intensity of tissue sections was scored in a 'blinded' manner.

60. Hill, R.C., Calle, E.A., Dzieciatkowska, M., Niklason, L.E. & Hansen, K.C. Quantification of extracellular matrix proteins from a rat lung scaffold to provide a molecular readout for tissue engineering. *Mol. Cell. Proteomics* **14**, 961–973 (2015).
61. Lopez, J.I., Kang, I., You, W.-K., McDonald, D.M. & Weaver, V.M. *In situ* force mapping of mammary gland transformation. *Integr. Biol. (Camb)* **3**, 910–921 (2011).
62. Pickup, M.W. *et al.* Stromally derived lysyl oxidase promotes metastasis of transforming growth factor-β-deficient mouse mammary carcinomas. *Cancer Res.* **73**, 5336–5346 (2013).
63. Bullen, A., Friedman, R.S. & Krummel, M.F. Two-photon imaging of the immune system: a custom technology platform for high-speed, multicolor tissue imaging of immune responses. *Curr. Top. Microbiol. Immunol.* **334**, 1–29 (2009).
64. Aguirre, A.J. *et al.* Activated Kras and Ink4a/Arf deficiency cooperate to produce metastatic pancreatic ductal adenocarcinoma. *Genes Dev.* **17**, 3112–3126 (2003).
65. Damiano, L. *et al.* Oncogenic targeting of BRM drives malignancy through C/EBPβ-dependent induction of α5 integrin. *Oncogene* **33**, 2441–2453 (2014).
66. Reinhart-King, C.A., Dembo, M. & Hammer, D.A. Endothelial cell traction forces on RGD-derivatized polyacrylamide substrata. *Langmuir* **19**, 1573–1579 (2003).
67. Lakins, J.N., Chin, A.R. & Weaver, V.M. *Methods Mol. Biol.* **916**, 317–350 (2012).
68. Paszek, M.J. *et al.* The cancer glycocalyx mechanically primes integrin-mediated growth and survival. *Nature* **511**, 319–325 (2014).
69. Mann, M.D., Crouse, D.A. & Prentice, E.D. Appropriate animal numbers in biomedical research in light of animal welfare considerations. *Lab. Animal Sci.* **41**, 6–14 (1991).